Particle encapsulation due to thread breakup in Stokes flow

M. G. BLYTH[1]† AND C. POZRIKIDIS[2]

[1]School of Mathematics, University of East Anglia, Norwich, NR4 7TJ, UK
[2]Department of Mechanical and Aerospace Engineering, University of California, San Diego,
La Jolla, CA 92093-0411, USA

The capillary instability of a liquid thread containing a regular array of spherical particles along the centreline is considered with reference to microencapsulation. The thread interface may be clean or occupied by an insoluble surfactant. The main goal of the analysis is to illustrate the effect of the particle spacing on the growth rate of axisymmetric perturbations and identify the structure of the most unstable modes. A normal-mode linear stability analysis based on Fourier expansions for Stokes flow reveals that, at small particle separations, the interfacial profiles are nearly pure sinusoidal waves whose growth rate is nearly equal to that of a pure thread devoid of particles. Higher harmonics suddenly enter the normal modes for moderate and large particle separations, elevating the growth rates and yielding a stability diagram that consists of a sequence of superposed pure-thread lobes. A complementary numerical stability analysis based on the boundary integral formulation for Stokes flow reveals the strong stabilizing effect of particles whose radius is comparable to the thread radius. Numerical simulations of the finite-amplitude motion based on the boundary integral method demonstrate that thread breakup leads to particles coated with annular layers of different thicknesses.

1. Introduction

Microencapsulation technology is of considerable interest in the food, biomedical, and pharmaceutical industry, where small particles, cells and cell agglomerates are produced and dispersed in an ambient medium. Microencapsulation techniques include droplet and emulsion formation, polyelectrolyte multi-layering and direct polymerization from a surface-adsorbed initiator. When applied to biological cells, many of these methods become limited by specifications of and constraints on chemical composition, uniformity and thickness of the membrane, polymerization scheme and maximum allowable shear stress. Encapsulation efficiency is of primary importance in the biomedical industry, as reviewed by Orive *et al.* (2003).

In one microencapsulation technique, a suspension of small particles, droplets, bubbles or cells is ejected through a micronozzle to form a liquid thread (e.g. Goosen *et al.* 1985). The Rayleigh capillary instability due to interfacial tension causes the thread to disintegrate into droplets that engulf the particles. Ideally, each droplet should engulf precisely one particle, so that solvent is not wasted, and the thickness

---

† Email address for correspondence: m.blyth@uea.ac.uk

of the coated liquid should be controlled by carefully selecting the nozzle diameter, physical properties of the materials and volume fraction of the suspension.

Hatziavramidis (2006) developed an efficient encapsulation device consisting of an encapsulation chamber that contains a two-layer water–oil system in which pancreatic islets are enclosed by a structurally stable, semi-permeable membrane into microcapsules. Cells or cell aggregates are fed in a single file by hydrodynamic focusing, thus ensuring separate encapsulation of individual islets. A valveless, diffuser-nozzle micropump transports the encapsulated islets out of the encapsulation chamber into a separation chamber in which the encapsulated islets are recovered by filtration or centrifugation. After the islets have been entrained into the withdrawal tube and coated, they are exposed to 514 nm light of an argon-ion laser to excite eosin-Y, initiate free-radical polymerization and produce a poly(ethylene glycol) (PEG) hydrogel. The thickness of the microcapsule shell enclosing an individual islet is controllable to within tens of a micron. The device can be used for coating particles of micron size with a structurally stable polymeric film but is particularly appropriate for group of or isolated living cells. In the case of islets, a thin but stable shell consisting of a selectively permeable, cross-linked polymer film encapsulates every single islet. Hatziavramidis & Pozrikidis (2007) studied the withdrawal hydrodynamics by analytical and numerical methods.

With a view towards establishing guidelines for controlling the microencapsulation process, in this work we consider the capillary instability of a liquid thread containing a coaxial array of evenly spaced spherical particles. In the limit of vanishing particle size, we obtain a pure liquid thread suspended in an infinite ambient fluid. The stability of the interface of the pure thread was studied by Tomotika (1935) for constant surface tension and by Kwak & Pozrikidis (2001) and others for varying surface tension due to an insoluble surfactant. Other researchers have considered the instability of an annular layer coated on the outside or inside of a circular cylinder. Although the former is somewhat relevant to the particle file configuration considered in the present work, it does differ considerably by permitting the growth of pure sinusoidal waves as normal modes.

In §2, the physical configuration and the main objectives of the analysis are discussed. In §3, a normal-mode linear stability analysis for Stokes flow is undertaken for axisymmetric disturbances. The perturbed interfacial position and flow variables are expanded in Fourier series whose fundamental wavenumber is determined by the particle spacing. Higher harmonic waves are naturally introduced due to the particle array, yielding normal modes with a distributed spectrum. The results reveal the paramount importance of higher harmonic components for sufficiently large particle separations. The linear stability analysis based on Fourier series becomes inaccurate for large particle radii and interfacial amplitudes.

In §4, a boundary integral formulation is presented for fluids with equal viscosity based on the periodic, axisymmetric Green's function of Stokes flow, and a numerical linear stability analysis is performed. The method is pivoted on the compatibility condition reconciling interfacial deformation and kinematics. The results complement and extend those of the Fourier series analysis by demonstrating the stabilizing effect of particles whose radius is comparable to that of the thread. Numerical solutions of the finite amplitude motion provide insights into the encapsulation process by illustrating the mechanisms of thread disintegration.

2. Problem formulation

We consider a cylindrical liquid thread with radius b and viscosity μ_1 suspended in an effectively infinite ambient fluid with viscosity μ_2. The viscosity ratio between the
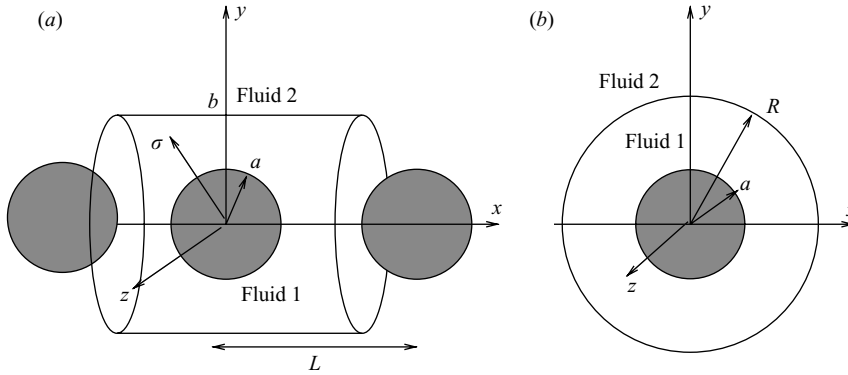
FIGURE 1. (*a*) An array of spherical particles is deployed along the centreline of a liquid thread. (*b*) The capillary instability leads to particle encapsulation.

fluids is $\lambda = \mu_2/\mu_1$. An array of evenly spaced spherical particles with radius $a < b$ is deployed along the centreline, as shown in figure 1. The densities of the two fluids are equal, and the particles are neutrally buoyant. The interface between the thread and the ambient fluid is occupied by an insoluble surfactant. The Rayleigh capillary instability due to interfacial tension causes the cylindrical thread to develop periodic corrugations of increasing amplitude and eventually disintegrate into an array of drops. We consider the instability subject to periodic axisymmetric perturbations whose wavelength is equal to the particle spacing L. Each period of the perturbation engulfs precisely one particle located at the crest of each period of the sinusoidal wave, as illustrated in figure 1.

Assume that the fluid contained in each period of the thread eventually separates from its neighbours, yielding an annular drop with outer radius R and inner radius a. In the absence of satellite drop formation causing thread loss, mass conservation requires

$$\frac{4\pi}{3} R^3 = \pi b^2 L. \tag{2.1}$$

The volumetric concentration of the suspension is $\phi = V_p/V_t = 4a^3/(3 b^2 L) = a^3/R^3$, where $V_p = 4\pi a^3/3$ is the particle volume and $V_t = \pi b^2 L$ is the volume occupied by one period of the thread. In practical applications, we want to specify the coating thickness $R - a$ and adjust the thread radius b so that (2.1) is satisfied with $L = L^*$, where L^* is the wavelength of the most unstable mode. A rough approximation can be obtained by overlooking the particles and identifying L^* with the most dangerous wavelength of the homogeneous thread. In the case of fluids with equal viscosity and in the absence of surfactants, $L^*/b \simeq 11.2$. Specifying $R = \alpha a$, we find $\phi = 1/\alpha^3$ and $b^2 = 4\alpha^3 a^3/(3L^*)$, where α is a coefficient that is greater than unity. For $\alpha = 2.5$, we find $b/a \simeq 1.23$, and for $\alpha = 2.0$, we find $b/a \simeq 0.98$, which is inadmissible. In fact, the simplified analysis predicts that $b/a > 1$ only for thick coatings, i.e. $\alpha > 2.04$.

Given these limitations, we proceed to study the precise effect of the particles on the most dangerous mode by carrying out a normal-mode linear stability analysis and then describe the process of breakup by numerical simulation.

3. Linear stability analysis by Fourier expansions

In the base state, two quiescent fluids are separated by a cylindrical interface with a circular cross-section. With reference to the cylindrical polar coordinate system illustrated in figure 1, we consider axisymmetric perturbations with period equal to the particle spacing, L, and describe the position of the interface using a Fourier series

$$\sigma = bf(x, t) \tag{3.1}$$

in which $f(x, t) = 1 + \epsilon \eta(x, t)$ and

$$\eta(x, t) = \sum_{m=1}^{\infty} A_m(t) \cos(mkx), \tag{3.2}$$

where $k = 2\pi/L$ is the fundamental wavenumber, A_m are dimensionless time-dependent coefficients and ϵ is a dimensionless number whose magnitude is small compared to unity. The centre of one arbitrary spherical particle in the infinite array has been placed at the origin of the x axis, as shown in figure 1. Since $b > a$, the dimensionless wavenumber is bounded by $kb < (b/a)\pi$.

The x and σ velocity components can be expressed in terms of the Stokes streamfunction for axisymmetric flow, ψ,

$$w^{(j)} = \frac{1}{\sigma} \frac{\partial \psi^{(j)}}{\partial \sigma}, \qquad u^{(j)} = -\frac{1}{\sigma} \frac{\partial \psi^{(j)}}{\partial x}, \tag{3.3}$$

where $j = 1$ for the thread and 2 for the ambient fluid. Inertial effects are assumed negligible, and the flows inside and outside the thread are governed by the linear equations of Stokes flow subject to suitable boundary conditions over the interface and particle surface.

We confine our attention to Stokes flow and introduce the Stokes streamfunction, satisfying the fourth-order partial differential equation

$$\mathcal{L}^4 \psi^{(j)} = 0, \tag{3.4}$$

for $j = 1, 2$, where

$$\mathcal{L}^2 \equiv \frac{\partial^2}{\partial \sigma^2} - \frac{1}{\sigma} \frac{\partial}{\partial \sigma} + \frac{\partial^2}{\partial x^2} \tag{3.5}$$

is a second-order differential operator (e.g. Pozrikidis 1997).

Following Wang & Skalak (1969), we express the streamfunction inside the thread as a superpositioning of a regular component described by a Fourier series and a singular component associated with rotational and irrotational singularities of axisymmetric Stokes flow represented by two sums,

$$\psi^{(1)}(x, \sigma, t) = \epsilon \frac{\gamma_0 b^2}{\mu_1} \left[\sum_{m=1}^{\infty} \left(B_m \frac{\sigma^2}{b^2} I_0(mk\sigma) + C_m \frac{\sigma}{b} I_1(mk\sigma) \right) \sin(mkx) \right.$$

$$\left. + \sum_{l=1}^{\infty} (D_l \mathcal{F}_l(x, \sigma) + E_l \mathcal{G}_l(x, \sigma)) \right], \quad (3.6)$$

where γ_0 is the surface tension of the unperturbed cylindrical interface; I_0 and I_1 are Bessel functions; and B_m, C_m, D_l and E_l are dimensionless time-dependent coefficients. The second sum on the right-hand side of (3.6) represents the flow induced by an infinite periodic array of singularities, yielding a flow that is symmetric with respect

to the origin of the x axis. The first set of singularities are derivatives of the point force, given by

$$\mathscr{F}_l(x, \sigma) \equiv \hat{\sigma}^2 \sum_{n=-\infty}^{\infty} \frac{\partial^{2l-1}}{\partial \hat{x}^{2l-1}} \left(\frac{1}{[\hat{\sigma}^2 + (\hat{x} - n\hat{L})^2]^{1/2}} \right) = -\hat{\sigma}^2 \frac{\partial^{2(l-1)} \mathscr{S}_3}{\partial \hat{x}^{2(l-1)}}, \qquad (3.7)$$

where $\hat{x} = x/b$, $\hat{\sigma} = \sigma/b$, $\hat{L} = L/b$ and

$$\mathscr{S}_3 \equiv \sum_{n=-\infty}^{\infty} \frac{\hat{x} - n\hat{L}}{[\hat{\sigma}^2 + (\hat{x} - n\hat{L})^2]^{3/2}}. \qquad (3.8)$$

The second set of singularities are derivatives of the point source, given by

$$\mathscr{G}_l \equiv \hat{\sigma}^2 \sum_{n=-\infty}^{\infty} \frac{\partial^{2l-1}}{\partial \hat{x}^{2l-1}} \left(\frac{1}{[\hat{\sigma}^2 + (\hat{x} - n\hat{L})^2]^{3/2}} \right) = -3\,\hat{\sigma}^2 \frac{\partial^{2(l-1)} \mathscr{S}_5}{\partial \hat{x}^{2(l-1)}}, \qquad (3.9)$$

where

$$\mathscr{S}_5 \equiv \sum_{n=-\infty}^{\infty} \frac{\hat{x} - n\hat{L}}{[\hat{\sigma}^2 + (\hat{x} - n\hat{L})^2]^{5/2}}. \qquad (3.10)$$

The functions $\mathscr{F}_l(x, \sigma)$ and $\mathscr{G}_l(x, \sigma)$ can be expressed in terms of sine Fourier series,

$$\mathscr{F}_l(x, \sigma) = \sum_{m=1}^{\infty} \mathscr{A}_{lm}(\sigma) \sin(mkx), \quad \mathscr{G}_l(x, \sigma) = \sum_{m=1}^{\infty} \mathscr{B}_{lm}(\sigma) \sin(mkx), \qquad (3.11)$$

where $\mathscr{A}_{lm}$ and $\mathscr{B}_{lm}$ are the corresponding Fourier coefficients.

Because of the assumed left-to-right symmetry with respect to the particle centre, the particles remain stationary. The no-slip and no-penetration conditions on the surface of the particle centred at the origin require

$$\psi^{(1)}(a\cos\theta, a\sin\theta, t) = 0, \quad \frac{\partial \psi^{(1)}}{\partial \sigma}(a\cos\theta, a\sin\theta, t) = 0, \qquad (3.12)$$

for $0 < \theta < \pi/2$.

Following Goren (1962), we express the general solution for the streamfunction in the ambient infinite fluid as

$$\psi^{(2)}(x, \sigma, t) = \epsilon \frac{\gamma_0 b^2}{\mu_1} \sum_{m=1}^{\infty} \left(F_m \frac{\sigma^2}{b^2} K_0(mk\sigma) + G_m \frac{\sigma}{b} K_1(mk\sigma) \right) \sin(mkx), \qquad (3.13)$$

where F_m, G_m are dimensionless time-dependent coefficients, and K_0, K_1 are Bessel functions. This expansion yields a quiescent fluid far from the thread, $\sigma \to \infty$.

To reconcile the thread and ambient flows, we introduce kinematic and dynamic conditions at the interface. Continuity of the radial and axial velocities requires the kinematic conditions

$$\psi^{(1)} = \psi^{(2)}, \quad \frac{\partial \psi^{(1)}}{\partial \sigma} = \frac{\partial \psi^{(2)}}{\partial \sigma} \qquad (3.14)$$

evaluated at $\sigma = bf(x, t)$. Substituting (3.6) and (3.13) and linearizing with respect to ϵ, we find

$$I_0(\hat{k}_m)B_m + I_1(\hat{k}_m)C_m - K_0(\hat{k}_m)F_m - K_1(\hat{k}_m)G_m$$
$$+ \sum_{l=1}^{\infty} (D_l \mathscr{A}_{lm}(b) + E_l \mathscr{B}_{lm}(b)) = 0, \qquad (3.15)$$

and

$$[2I_0(\hat{k}_m) + m\hat{k}I_1(\hat{k}_m)]B_m + \hat{k}_m I_0(\hat{k}_m)C_m + [\hat{k}_m K_1(\hat{k}_m) - 2K_0(\hat{k}_m)]F_m$$
$$+ \hat{k}_m K_0(\hat{k}_m)G_m + \sum_{l=1}^{\infty}(D_l \mathscr{A}'_{lm}(b) + E_l \mathscr{B}'_{lm}(b)) = 0, \qquad (3.16)$$

where $\hat{k}_m = mkb$. Kinematic compatibility requires $\mathrm{D}(\sigma - bf)/\mathrm{D}t = 0$, where $\mathrm{D}/\mathrm{D}t$ is the material derivative. Linearizing and simplifying, we find

$$\frac{\partial f}{\partial t} = u^{(2)} \qquad (3.17)$$

at $\sigma = bf(x,t)$. Substituting (3.2) and (3.13), we derive a system of differential equations,

$$\frac{\mathrm{d}A_m(t)}{\mathrm{d}t} = -\frac{\gamma_0}{\mu_1}\hat{k}_m(K_0(\hat{k}_m)F_m + K_1(\hat{k}_m)G_m). \qquad (3.18)$$

3.1. Surfactant transport

The interface is occupied by an insoluble surfactant with surface concentration $\Gamma(x,t)$ governed by the convection–diffusion equation

$$\frac{\mathrm{d}\Gamma}{\mathrm{d}t} = w\frac{\partial \Gamma}{\partial l} - \frac{1}{\sigma}\frac{\partial(\sigma u_t \Gamma)}{\partial l} - 2\kappa_m u_n \Gamma + \frac{D_s}{\sigma}\frac{\partial}{\partial l}\left(\sigma\frac{\partial \Gamma}{\partial l}\right), \qquad (3.19)$$

where l is the arclength along the trace of the interface in a meridional plane; t is the unit tangent vector pointing in the direction of increasing arclength l; $\kappa_m \equiv 1/2\,\nabla\cdot\boldsymbol{n}$ is the mean curvature; $u_t = \boldsymbol{u}\cdot\boldsymbol{t}$ and $u_n = \boldsymbol{u}\cdot\boldsymbol{n}$ are the tangential and normal interfacial velocities with the unit normal vector $\boldsymbol{n}$ pointing into the thread (e.g. Li & Pozrikidis 1997; Yon & Pozrikidis 1998). In practice, the surfactant diffusivity D_s is very small, and the diffusion term in (3.19) makes a negligible contribution. The derivative $\mathrm{d}/\mathrm{d}t$ on the left-hand side of (3.19) expresses the rate of change of a variable following the motion of an interfacial marker point moving normal to the interface and with an arbitrary tangential velocity $w(l)$. If $w = u_t$, the marker points are Lagrangian point particles moving with the fluid velocity.

Assuming that the surfactant concentration is sufficiently far below the saturation level, we adopt Gibbs's linear equation of state $\gamma_c - \gamma = \Gamma E$ relating the local surface tension to the surfactant concentration, where E is the surface elasticity, and γ_c is the surface tension obtaining at a clean interface free of surfactant (e.g. Pozrikidis 2004). Alternatively, the law may be expressed as

$$\gamma = \frac{\gamma_0}{1-\beta}\left(1 - \beta\frac{\Gamma}{\Gamma_0}\right), \qquad (3.20)$$

where Γ_0 is a reference surfactant level, and $\beta = \Gamma_0 E/\gamma_c$ is a physio-chemical parameter. We will present results with reference to the dimensionless Marangoni number, defined by

$$Ma = \frac{\beta}{1-\beta}. \qquad (3.21)$$

When $Ma = 0$, the surface is clean, and the surface tension is constant along the interface.

In the linear stability analysis, the surface tension and surfactant concentration are expressed as perturbations of their base state values,

$$\gamma = \gamma_0(1 + \epsilon\hat{\gamma}), \qquad \hat{\gamma} = \sum_{m=1}^{\infty} \gamma_m(t)\sin(mkx), \tag{3.22}$$

$$\Gamma = \Gamma_0(1 + \epsilon\hat{\Gamma}), \qquad \hat{\Gamma} = \sum_{m=1}^{\infty} \Gamma_m(t)\sin(mkx), \tag{3.23}$$

where $\hat{\gamma}$, $\hat{\Gamma}$ are dimensionless functions, and γ_m, Γ_m are dimensionless coefficients. The linearized form of (19), the surfactant transport equation, is given by (e.g. Blyth & Pozrikidis 2004),

$$\frac{\partial\hat{\Gamma}}{\partial t} + \left(\frac{\partial w^{(2)}}{\partial x} + \frac{u^{(2)}}{b}\right) = D_s\frac{\partial^2\hat{\Gamma}}{\partial x^2}, \tag{3.24}$$

where all terms are evaluated at the unperturbed position, $\sigma = b$. Substituting (3.22) and (3.13), we find

$$\frac{\mathrm{d}\Gamma_m}{\mathrm{d}t} + m^2k^2D_s\Gamma_m = \frac{\gamma_0}{\mu_1}mk((F_m - \hat{k}_mG_m)\,K_{0m} - (\hat{k}_mF_m + G_m)\,K_{1m}), \tag{3.25}$$

where $K_{0m} = K_0(\hat{k}_m)$, and $K_{1m} = K_1(\hat{k}_m)$.

3.2. *Dynamic interfacial conditions*

A second set of interfacial conditions arises by balancing the stress on either side of the interface and the surface tension, yielding

$$\left(\boldsymbol{\sigma}^{(1)} - \boldsymbol{\sigma}^{(2)}\right)\cdot\boldsymbol{n} = \gamma\,2\kappa_m\boldsymbol{n} - \frac{\partial\gamma}{\partial l}\boldsymbol{t}, \tag{3.26}$$

evaluated at $\sigma = bf(x, t)$, where $\boldsymbol{\sigma}^{(j)}$ is the Newtonian stress tensor in the jth fluid. The final term on the right-hand side of (3.26) is the Marangoni traction due to local variations in the surface tension associated with the presence of the surfactant.

A linear normal stress balance arises by taking the dot product of (3.26) with the unit normal vector, $\boldsymbol{n}$, to obtain $p_0^{(1)} - p_0^{(2)} = \gamma_0/b$, where the subscript 0 denotes the basic quiescent state. Making substitutions and eliminating the pressure using the Stokes equation, we find

$$\left[2\mu_j\frac{\partial^2 u^{(j)}}{\partial\sigma\,\partial x} - \mu_j\nabla^2 w^{(j)}\right]_2^1 = \gamma_0\left(\frac{f_x}{b^2} + f_{xxx}\right) - \frac{\gamma_0}{b}\frac{\partial\hat{\gamma}}{\partial x}, \tag{3.27}$$

evaluated at $\sigma = b$, where $[\cdot]_2^1 = [\cdot]_1 - [\cdot]_2$ signifies a discontinuity across the interface. The linearized form of the tangential stress balance takes a similar form,

$$\left[\mu_j\left(\frac{\partial w^{(j)}}{\partial\sigma} + \frac{\partial u^{(j)}}{\partial x}\right)\right]_2^1 = \gamma_0\frac{\partial\hat{\gamma}}{\partial x} \tag{3.28}$$

evaluated at $\sigma = b$. Substituting the Fourier expansions for the velocity and surface tension and using Gibbs's law (3.20) to eliminate the surface tension in favour of the surfactant concentration, we derive normal and tangential stress balances

$$2\hat{k}_m^2 I_1(\hat{k}_m)B_m + 2\hat{k}_m[\hat{k}_m I_0(\hat{k}_m) - I_1(\hat{k}_m)]C_m + 2\lambda\hat{k}_m^2 K_1(\hat{k}_m)F_m + 2\lambda\hat{k}_m[\hat{k}_m K_0(\hat{k}_m)$$

$$+ K_1(\hat{k}_m)]G_m + \left[1 - \hat{k}_m^2\right]A_m + Ma\,\Gamma_m = 2\hat{k}_m\sum_{l=1}^{\infty}(D_l\mathscr{A}_{lm} + E_l\mathscr{B}_{lm}) \tag{3.29}$$

and

$$2[I_1(\hat{k}_m) + \hat{k}_m I_0(\hat{k}_m)] B_m + 2\hat{k}_m I_1(\hat{k}_m) C_m + 2\lambda[K_1(\hat{k}_m) - \hat{k}_m K_0(\hat{k}_m)] F_m$$
$$- 2\lambda \hat{k}_m K_1(\hat{k}_m) G_m - Ma\, \Gamma_m + \hat{k}_m \sum_{l=1}^{\infty} (D_l \mathscr{A}_{lm} + E_l \mathscr{B}_{lm}) = 0, \quad (3.30)$$

where $\hat{k} = kb$.

3.3. *Normal modes*

With a view to identifying normal modes, we seek exponentially growing or decaying solutions in the form

$$(A_m,\ B_m,\ C_m,\ F_m,\ G_m,\ \Gamma_m) = e^{st}(\tilde{A}_m,\ \tilde{B}_m,\ \tilde{C}_m,\ \tilde{F}_m,\ \tilde{G}_m,\ \tilde{\Gamma}_m) \quad (3.31)$$

and

$$(D_l,\ E_l) = e^{st}(\tilde{D}_l,\ \tilde{E}_l), \quad (3.32)$$

for $l = 1, 2, \ldots$, where s is an unknown growth rate. Substituting these expressions in (3.18) and (3.25), we obtain

$$s\tilde{A}_m = -\frac{\gamma_0}{\mu_1}\hat{k}_m(K_0(\hat{k}_m)\tilde{F}_m + K_1(\hat{k}_m)\tilde{G}_m) \quad (3.33)$$

and

$$(s + m^2 k^2 D_s)\tilde{\Gamma}_m = \frac{\gamma_0}{\mu_1}mk([\tilde{F}_m - \hat{k}_m\tilde{G}_m]K_{0m} - [\hat{k}_m\tilde{F}_m + \tilde{G}_m]K_{1m}). \quad (3.34)$$

The continuity conditions (3.15) and (3.16) and the interfacial stress balances (3.29) and (3.30) remain the same, provided that tildes are inserted over the unknown coefficients.

We derived a system of six homogeneous equations for each Fourier mode m. The set of equations for each Fourier mode is coupled with corresponding sets for all other Fourier modes through the no-slip and no-penetration conditions over the spherical particles, expressed by (3.12). Only in the absence of the particles are the Fourier modes also normal modes.

The eigenvalue problem was solved numerically to obtain the growth rates of normal modes. A set of N collocation points is introduced around the contour of the sphere in a meridional plane at the meridional angles $\theta_i = (\pi/2)(1 - i/(N + 1))$, where $i = 1, \ldots, N$. Enforcing the no-slip and no-penetration conditions (3.12) yields a set of $2N$ algebraic equations. Next, the Fourier series (3.6) and (3.13) are truncated after M terms, furnishing a further set of $6M$ equations comprising the interfacial conditions. Finally, the infinite series in (3.29) and (3.30) are truncated after N terms to obtain a set of $6M + 2N$ equations for the $6M + 2N$ unknown coefficients. The computation of the sum in (3.8) is expedited by applying the Aitken extrapolation method for a series with quadratic decay (e.g., Pozrikidis 2008). Because of the quartic decay of the series in (3.10), the sum can be computed efficiently by direct summation. The derivatives of $\mathscr{S}_3$ and $\mathscr{S}_5$ in (3.8) and (3.10) were computed using recurrence formulae presented in Appendix A. The Fourier coefficients in the expansions in (3.11) were computed by a fast Fourier transform (FFT). Assembling the full set of equations, we derive a generalized matrix eigenvalue problem expressed by

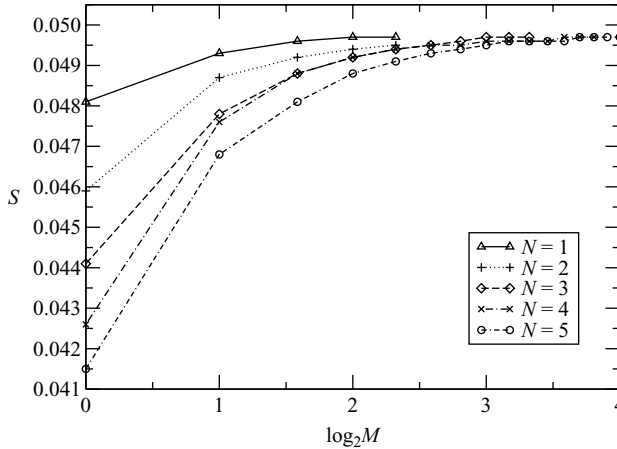$$\boldsymbol{A} \cdot \boldsymbol{x} = s\boldsymbol{B} \cdot \boldsymbol{x}, \quad (3.35)$$

FIGURE 2. Graphs of the dominant growth rates, $S = (\gamma_0/b\mu_1)s$, for various truncation levels, M and N, for a case with $kb = 0.45$, $a/b = 0.2$, $\lambda = 0.5$ and $Ma = 0$.

where $\boldsymbol{A}$ and $\boldsymbol{B}$ are $(6M + 2N) \times (6M + 2N)$ coefficient matrices, and $\boldsymbol{x} = (\tilde{A}_1, \tilde{B}_1, \tilde{C}_1, \tilde{F}_1, \tilde{G}_1, \tilde{\Gamma}_1, \ldots, \tilde{A}_M, \tilde{B}_M, \tilde{C}_M, \tilde{F}_M, \tilde{G}_M, \tilde{\Gamma}_M, D_1, E_1, \ldots, D_N, E_N)^T$ is the vector of unknowns. The solution was found numerically using the Numerical Algorithms Group (NAG) Fortran Library code F02GJF implementing the QZ algorithm. A typical calculation with $N = M = 5$ takes around $10\,\mathrm{s}$ on a $2\,\mathrm{GHz}$ processor running Linux. The CPU time rapidly escalates for larger values of N and M.

To illustrate the accuracy of the numerical method, we consider a thread with a clean interface, i.e. $Ma = 0$, and introduce the dimensionless growth rate, $S = \gamma_0 s/b\mu_1$. Figure 2 shows the dominant growth rate for a sample case with moderate wavenumber, $kb = 0.45$, for $a/b = 0.2$ and $\lambda = 0.5$. The FFT was performed with $N_F = 2^6 = 64$ Fourier modes. Computed values are shown for several Fourier truncation levels, M, and different numbers of collocation points around the particle contour, N. The results reveal that good accuracy for small particles and moderate wavenumbers can be obtained with a low or moderate truncation level. Smaller wavenumbers, with kb smaller than about 0.4, require higher numerical resolution.

The results presented in §4 for moderate wavenumbers were obtained with $N = 4$, $M = 7$ and $N_F = 2^6$. Results for smaller wavenumbers were obtained using truncation levels up to $N = 7$, $M = 30$ and $N_F = 8$. For large particles, with a/b greater than about 0.2, a large number of collocation points are required, demanding a large value of N and the consequent computation of high-order derivatives of the point force and point source terms in (3.7) and (3.9). In numerical practice, this leads to unacceptable levels of error that undermine the accuracy of the calculations. An alternative approach based on the boundary integral method for Stokes flow capable of producing accurate results for particles with $a/b > 0.2$ is presented in §5.

4. Results and discussion

A pure thread devoid of particles admits one stable, unstable or neutrally stable normal mode for a fixed wavenumber kb in the absence of surfactants, i.e. $Ma = 0$ (Tomotika 1935). When the thread is loaded with particles, multiple normal modes arise for any given set of parameters, and the interfacial shape for each mode is no
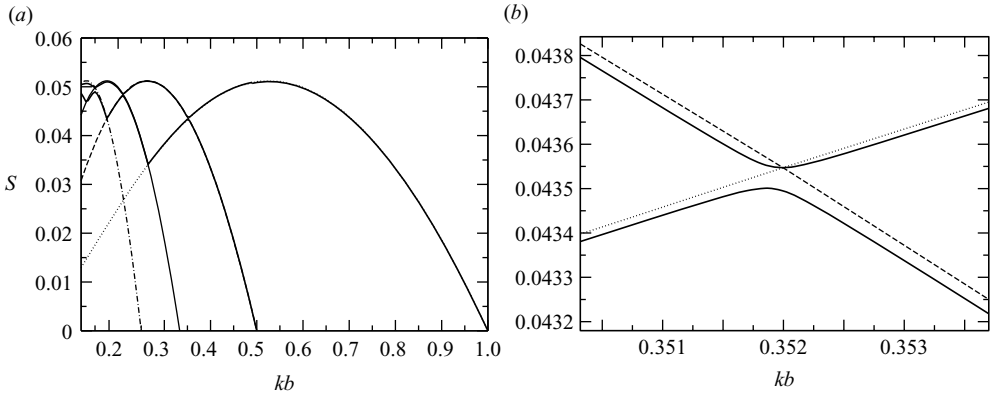
FIGURE 3. (*a*) Growth rates of the two dominant modes for $a/b = 0.2$, $\lambda = 0.5$ and $Ma = 0$; (*b*) close-up of (*a*). The growth rate of a pure thread and its first three higher harmonics are shown as thin dotted, thin broken, thin solid and thin dot-dashed lines, respectively.

longer a pure Fourier mode. However, in all cases, instability occurs only below the critical Rayleigh threshold of unity, i.e. when $kb < 1$.

Figure 3(*a*) shows graphs of the growth rate of the two dominant modes for a thread suspended in a less viscous fluid, $\lambda = 0.5$, and a clean interface, $Ma = 0$. The particle radius is five times smaller than the thread radius, i.e. $a/b = 0.2$. The dominant growth rates of the pure thread are depicted as thin lines, and the dominant growth rates of the loaded thread are depicted as thick lines. The thin broken, solid and dot-dashed lines show stability graphs for the first few higher harmonic disturbances of the pure thread whose wavelength is equal to an integral fraction of the particle spacing, i.e. $L/2$, $L/3$ and $L/4$.

The results show that the most dangerous modes of the loaded thread overlap with those for a pure thread. As kb decreases from the Rayleigh threshold of unity, the dominant loaded-thread modes lock on to the fundamental pure-thread mode and its first higher harmonic. The growth rate for the fundamental mode coincides with the growth rate for its first higher harmonic at $\hat{k} = 0.352$. At this crossover point, the dominant loaded-thread mode jumps from the fundamental pure-thread mode to its first higher harmonic. Simultaneously, the second most dangerous loaded-thread mode jumps from the first higher harmonic to the fundamental mode. The interchange is shown in close-up in figure 3(*b*).

Physically, the particles allow all higher harmonics of the fundamental wavenumber determined by the particle spacing to enter the normal modes and thereby permit the most unstable available higher harmonic waves of the pure thread to dominate the motion. Corroborative evidence is presented in figure 4 showing the interfacial deflection of the most unstable normal modes, $\tilde{\eta} \equiv \eta e^{-st}$, at $kb = 0.4$ and 0.3. The first wavenumber, $kb = 0.4$, lies on the right of the transition point at $kb = 0.35199737$, where the pure modes shown with broken and dotted lines in figure 3(*b*) intersect. The second wavenumber, $kb = 0.3$, lies on the left of the transition point. The deflections are normalized so that $\tilde{\eta}(0) = 1$. The Fourier coefficients for each profile are presented in table 1 accurate to two decimal places. Evidently, the deflection for $kb = 0.4$ is almost a pure cosine wave with wavelength L, and the deflection for $kb = 0.3$ is almost a pure cosine wave with wavelength $L/2$.

In both cases described in figure 4, the interfacial profiles are virtually indistinguishable from the sinusoidal profiles for a pure thread. The profile for

kb	A_1	A_2	A_3	A_4
0.4	1	0	0	0
0.3	0	1	0	0

TABLE 1. Interfacial displacement coefficients of the normal modes, A_m, corresponding to the graphs shown in figure 4 for $a/b = 0.2$, $\lambda = 0.5$ and $Ma = 0$.
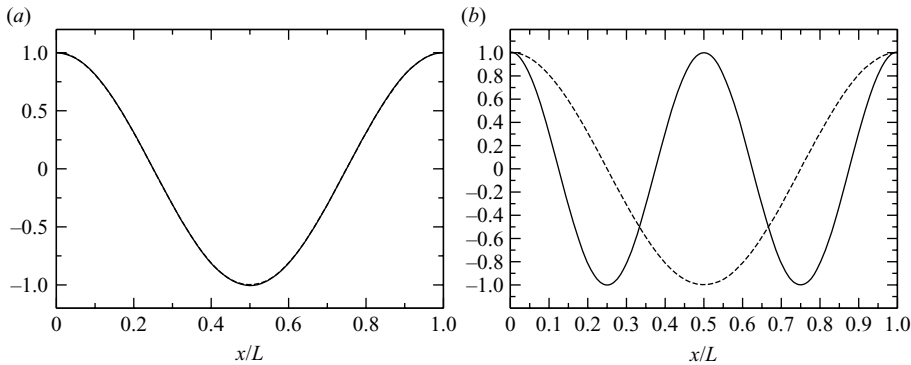

FIGURE 4. Linear interfacial deflection $\tilde{\eta}$ for $a/b = 0.2$, $\lambda = 0.5$, $Ma = 0$ and (a) $kb = 0.40$, (b) $kb = 0.3$. The particle is located at $x/L = 0$.

$kb = 0.4$ is almost identical to the fundamental pure wave, and the profile for $kb = 0.3$ is almost identical to the first higher harmonic of the pure wave. As the particle size tends to zero, the presence of the particles becomes significant insofar as to determine the fundamental wavenumber, and the stability graph consists of an infinite sequence of the fundamental and superharmonic lobes of the pure thread. It is intriguing that for the small but not infinitesimal particle size considered in figure 4, the transition from the fundamental to the first higher harmonic mode occurs suddenly with respect to the wavenumber. In §5, we will see that for particles with larger size, the transition from lobe to lobe is smoother.

Accurate numerical computation becomes increasingly difficult as the wavenumber decreases. However, the results show that for small particles, with a/b smaller than 0.2, the growth rates of loaded-thread normal modes coincide with those of a pure thread and jump from one pure-thread mode to its immediate higher harmonic at the pure-thread intersections. Guided by this observation, we trace the behaviour of the growth rates at small wavenumber by following the intersections of the growth rates for the pure-thread modes. Figure 5(a) displays the wavenumbers at which pure-thread modes with wavelength $2\pi/(mk)$ and $2\pi/[(m+1)k]$ intersect for increasing values of the integer index m. The results for a clean thread, with $Ma = 0$, are shown with circles on a solid line.

As m increases, the wavenumber approaches zero at a rate that is proportional to $1/m$. At each intersection, the pure mode with the shorter of the two wavelengths dominates the interfacial deflection. In fact, the loaded thread behaves just as though the particles were absent. For example at the intersection between the thin solid and the thin broken line in figure 3(a), which although not clearly visible in the figure occurs at $kb = 0.21078$, accurate calculations using up to $N = 16$ collocation points reveal that the growth rate is almost entirely insensitive to the particle radius over

λ	Ma	kb	S
0.10	0	0.2786	0.090
0.25	0	0.3239	0.062
0.50	0	0.3520	0.044
0.50	1	0.3832	0.031
0.50	2	0.3946	0.029
1	0	0.3728	0.029
10.0	0	0.3789	0.009

TABLE 2. Resonant growth rates S and corresponding pure-mode intersection wavenumbers kb for various values of λ and Ma.
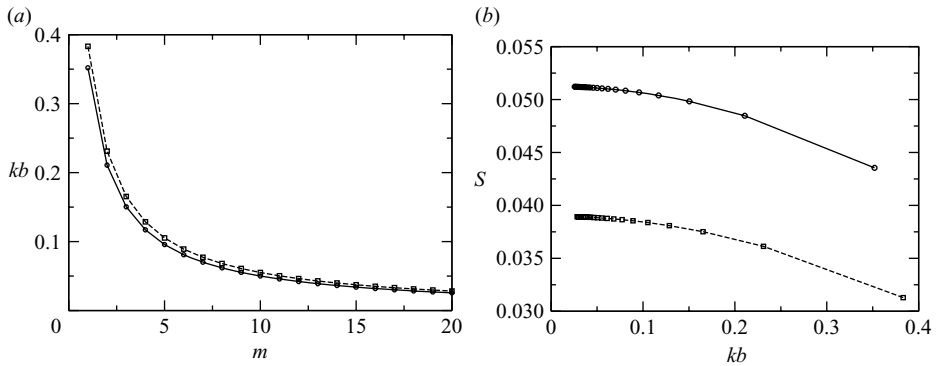

FIGURE 5. (*a*) The wavenumbers at the points of intersection between the pure-thread modes with wavelength $2\pi/(mk)$ and $2\pi/[(m+1)k]$ for $\lambda = 0.5$, $Ma = 0$ (circles on a solid line) and $\lambda = 0.5$, $Ma = 1$ (squares on a broken line). (*b*) Corresponding growth rates at the wavenumbers in (*a*).

the range $a/b = 0.2$ up to $a/b = 0.8$, changing by less than 0.1 %. A similar remark holds for the intersection between the thin solid line and the thin dot-dashed line in figure 3(*a*), where $kb = 0.15047$. Again, the growth rate is virtually independent of the particle radius over the range $a/b = 0.2$ up to $a/b = 0.8$, changing by less than 0.2 %. Indeed, this phenomenon appears to be independent of the choice of parameter values. In table 2 we show the resonant growth rates S at sample pure-mode intersection wavenumbers for a selection of different values of λ and Ma. In each case, we have checked that the growth rate is identical to the precision shown for each of the particle sizes $a/b = 0.2, 0.4, 0.6$ and 0.8. In general, the particles are expected to influence the thread dynamics more actively as a/b increases. This will be demonstrated in §5 through a boundary integral stability analysis and simulations. The growth rates at the wavenumbers of intersection are shown in figure 5(*b*). It appears that as kb approaches zero, the growth rate tends to a finite limit.

Suppose that the interfacial waves lead to thread breakup into drops. If the fundamental wave is the most unstable, all particles will be encapsulated, and no pure drops will develop, apart from small satellite drops. If the first higher harmonic wave is the most unstable, all particles will be encapsulated, and an alternating sequence of drops will develop. If the mth higher harmonic is the most unstable, a sequence of $m - 1$ drops will develop, interrupted by a sequence of coated particles. To estimate the outer shell radius of the encapsulated particles, we may assume that L is the most
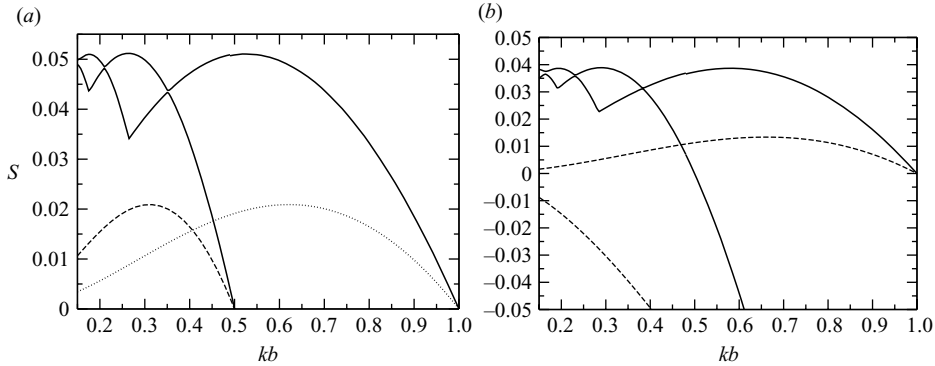
FIGURE 6. Comparison of the growth rates of a loaded thread with $a/b = 0.2$ and $\lambda = 0.5$ and an annular thread with viscosity $\mu_2 = 0.5\mu_1$ coating a cylinder of radius $0.2b$. The dominant growth rates for a loaded thread shown as thick solid lines. (a) Results for a clean interface, $Ma = 0$. The dominant growth rate and its first higher harmonic for an annular thread are shown as thin dotted and thin broken lines, respectively. (b) Results in the presence of a surfactant with $Ma = 1$ and $D_s = 0$. The dominant growth rates for an annular thread are shown as thin broken lines.

unstable wavenumber for a pure thread corresponding to $2\pi bm/L \simeq 0.526$ when $\lambda = 0.5$ and consider a modification of (2.1),

$$\frac{4}{3}\pi R^3 = \frac{\pi b^2 L}{m}\chi_m, \tag{4.1}$$

where χ_m expresses the volume fraction of liquid apportioned to the particles determined by the structure of the normal modes, and $\chi_1 \simeq 1$. Rearranging, we find

$$\frac{R}{b} = \left(\frac{6\pi\chi_m}{4 \times 0.526}\right)^{1/3}. \tag{4.2}$$

In §5, we will see that χ_m strongly depends on the precise form of an imposed perturbation.

It is of interest to compare the results for a thread loaded with a sequence of spherical particles with those for an annular viscous thread coated on the outside of a circular cylinder. For illustration, we consider a cylinder with the same diameter as the spherical particles. Figure 6(a) shows as thick solid lines the two dominant growth rates for the case of a thread with a clean interface, $Ma = 0$, loaded with particles whose radius is five times smaller than the thread radius, $a/b = 0.2$, and suspended in a less viscous fluid, $\lambda = 0.5$. The growth rates for a clean annular thread with viscosity μ_1 coating a circular cylinder of radius $0.2b$ and surrounded by an ambient viscous fluid with viscosity $\mu_2 = 0.5\mu_1$ is depicted with a thin dotted line. The growth rate for the first higher harmonic is shown with a thin broken line. The growth rates for the annular film were computed using the method described by Kwak & Pozrikidis (2001). The results show that the growth rates for the loaded thread are substantially higher than those for the annular thread. The two sets of growth rates differ the most when kb is small, and the particles are widely spaced.

In the presence of an insoluble surfactant, a homogeneous thread devoid of particles admits two normal modes for a fixed wavenumber, kb (e.g., Kwak & Pozrikidis
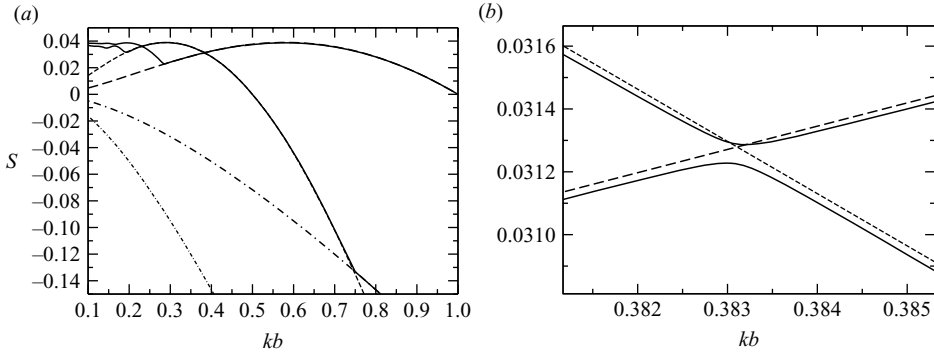
FIGURE 7. (a) Growth rates for $a/b = 0.2$, $\lambda = 0.5$, $Ma = 1$ and $D_s = 0$. Panel (b) shows a close-up of (a). The dominant growth rates for a loaded thread are shown as thick solid lines, and those for a pure thread are shown as broken and dot-dashed lines, with the thin lines representing the first higher harmonics.

2001). Figure 7(a) shows with thick solid lines the dominant growth rates for a contaminated thread loaded with particles for $\lambda = 0.5$, $b/a = 0.2$, $Ma = 1$ and $D_s = 0$. The corresponding growth rates for a pure thread are shown with thick broken lines and thick dot-dashed lines. The thin broken and thin dot-dashed lines graph the first higher harmonics of the respective pure modes. The growth rate curves are qualitatively similar to those for a clean thread displayed in figure 3. Again, for the small particle size presently considered, the growth rates for the loaded thread overlap with those for a pure thread. Moreover, the dominant loaded-thread mode jumps from one pure-thread mode to its higher harmonic at the wavenumber at which these two intersect. A close-up of the crossover at $kb = 0.383$ is shown in figure 7(b).

The second most dangerous mode of the contaminated thread attaches to the fundamental unstable pure mode at $kb = 0.284$ before crossing to the first higher harmonic pure mode at $kb = 0.383$. It overlaps with this mode until $kb = 0.745$ at which it jumps to the second most dangerous pure mode. Overall, the surfactant shifts the growth rate curves for the loaded thread downwards, tending to stabilize the thread. However, the unstable range of wavenumbers remains unchanged. As for a clean thread, we may estimate the growth rate at small wavenumber by considering the intersections of the pure-thread modes. In figure 5, we show the wavenumbers and growth rates at the intersections of the dominant pure modes for a contaminated thread with $Ma = 1$. The results are shown with squares on a broken line. As the wavenumber tends to zero, the growth rate approaches a finite value.

Figure 6(b) compares the growth rates of the loaded thread with those of an annular layer coated on the outside a cylinder whose radius is equal to the particle radius, for $Ma = 1$ and $D_s = 0$. The two dominant modes of the annular layer are both shown as broken lines. As in the case of the pure thread, the differences between the two sets of results is striking, particularly for small values kb and widely spaced spherical particles.

The results discussed in this section are representative of the general behaviour of the system. Investigations carried out for numerous different values of the parameters λ and Ma all led to qualitatively similar results to those presented here.

5. Boundary integral formulation

In the case of fluids with equal viscosity and a clean interface devoid of surfactants, the boundary integral formulation for axisymmetric Stokes flow provides us with an integral representation for the velocity at a point, x_0, inside or outside the thread,

$$u_\alpha(x_0) = -\frac{\gamma}{4\pi\mu} \int_I G_{\alpha\beta}(x, x_0) 2\kappa_m(x) n_\beta(x) \mathrm{d}l(x)$$

$$-\frac{1}{8\pi\mu} \int_P G_{\alpha\beta}(x, x_0) f_\beta(x) \mathrm{d}l(x), \quad (5.1)$$

where I is one period of the interfacial contour in a meridional plane; P is the contour of one particle in an meridional plane; f is the particle surface traction; l is the arclength; and $G_{\alpha\beta}(x_0, x)$ is the periodic Green's function of axisymmetric Stokes flow discussed in Appendix B. Greek indices take the values x or σ for the axial or radial direction. In the absence of particles, the second integral on the right-hand side of (5.1) does not appear. Applying (5.1) to the particle contour, we obtain an integral equation of the first kind for the surface traction.

To solve the integral equation and thus retrieve the interfacial velocity, we divide one period of the interface in an meridional plane into N_I intervals and approximate the interfacial shape using cubic spline interpolation with respect to the polygonal arclength, subject to periodic boundary conditions (e.g. Pozrikidis 2008). The mean curvature and normal vector follow readily from the parametric interpolation. The contour of a spherical particle in a meridional plane is divided into N_p circular elements, and the traction components are approximated with constant functions over each element. Pointwise collocation is then enforced at the midpoints of the circular elements to derive a system of linear equations for the element tractions. The integrals over the boundary elements are computed using the six-point Gauss–Legendre quadrature after the logarithmic singularity of the diagonal components of the Green's function has been subtracted out and then integrated analytically with respect to the meridional angle.

The calculation of the singe-layer integral over the interface requires careful attention due to the pronounced sensitivity of the numerical linear stability analysis discussed in the next section on the accurate evaluation of the integrals. In one method, the integration is performed over straight segments connecting pairs of successive interfacial nodes after the logarithmic singularity of the diagonal components of the Green's function has been subtracted out and then integrated analytically with respect to the straight distance from the singular point. In the second approach, an integral identity is used to restate the single-layer potential over the interface in the desingularized form

$$\int_I G_{\alpha\beta}(x, x_0) 2 [\kappa_m(x) - \kappa_m(x_0)] n_\beta(x) \mathrm{d}l(x), \quad (5.2)$$

and the integration is performed with respect to the polygonal arclength implementing the cubic spline interpolation (e.g. Pozrikidis 1992). For a fixed number of boundary elements, approximating the interfacial contour with a polygonal line using the first method may introduce spurious unphysical eigenvalues that disappear as the discretization level increases; and for this reason the second approach is far superior.

5.1. Numerical linear stability analysis

We have seen that the cylindrical interface is susceptible to a capillary instability mediated by exponentially growing disturbances representing normal modes. In the

case of axisymmetric perturbations with period equal to the particle spacing, L, the interfacial shape is described by

$$\sigma = \Sigma(x, t) = b[1 + \eta(x) \exp(st)], \tag{5.3}$$

where $\eta(x)$ is a periodic eigenfunction with small amplitude representing a normal mode, and s is the corresponding growth rate. In the absence of a mean flow, kinematic compatibility requires the linearized condition

$$\frac{\partial \Sigma}{\partial t} = u_\sigma(\Sigma, t) \tag{5.4}$$

evaluated at the interface. Substituting the normal-mode waveform, evaluating the velocity at the initial instant and rearranging, we find

$$u_\sigma[b(1 + \eta), t = 0] = sb\eta(x). \tag{5.5}$$

In its discrete representation in terms of interfacial marker points, this equation evaluated at the ith marker point, x_i, becomes

$$u_\sigma(x_i; x_1, x_2, \ldots, x_{N_I}; t = 0) = sb\eta_i, \tag{5.6}$$

where $i = 1, \ldots, N_I$, and we have denoted $\eta_i = \eta(x_i)$. Linearizing the velocity on the left-hand side with respect to the small displacements of the marker points, we find

$$\left(\frac{\partial u_\sigma}{\partial \eta_j}\right)_{\eta=0} (x_i)\eta_j = s\eta_i, \tag{5.7}$$

which shows that the growth rate is an eigenvalue of the matrix of derivatives, M, on the left-hand side. The matrix M is singular, having a zero eigenvalue with a corresponding constant eigenvector representing a physically inadmissible radial expansion.

The boundary integral formulation can be used to perform a numerical normal-mode linear stability analysis. The numerical procedure involves the following steps:

(*a*) Divide one period of the straight interfacial contour into N_I arbitrary intervals separated by nodes.

(*b*) Compute and store the radial velocity at the position of all nodes. In principle, the radial velocity of a cylindrical column with uniform mean curvature is zero; in practice, the radial velocities are non-zero due to approximations in the computation of the contour integral with non-zero curvature.

(*c*) Displace the ith interfacial node and its periodic images along the σ axis by the small distance $b\epsilon$, for $i = 1, \ldots, N_I$.

(*d*) Compute the radial velocity at the position of all nodes; subtract the velocity computed in (*b*); divide the difference by $b\epsilon$; and put the result at the ith row of a matrix, M.

The growth rates of a fundamental perturbation with wavelength L and its higher harmonics with wavelengths L/m are the eigenvalues of M, where m is an integer. The corresponding eigenvectors are discrete representations of the normal-mode eigenfunctions, $\eta(x)$.

Full advantage is taken of the left-to-right symmetry of the flow with respect to the plane that passes through each particle centre normal to the x-axis to reduce the size of the eigensystem. Even with this improvement, the solution of the eigenvalue problem for each configuration takes from 15 minutes to many hours of CPU time on a high-end workstation. All results reported in this section were obtained using the spline interpolation for integrating over the interface.

(a)

kb	ϵ	N_G	$N_I = 8$	16	32	64	96	128	∞	Mode
2/3	10^{-3}	4	0.0312	0.0321	0.0300					F
	10^{-6}	4	0.0313	0.0328	0.0332	0.0334			0.0334	F
0.3	10^{-6}	3	0.0252	0.0238	0.0237	0.0237	0.0237		0.0237	F
			0.0320	0.0337	0.0347	0.0351	0.0352		0.0352	S1
0.37276613	10^{-6}	3	0.0297	0.0290	0.0290	0.0291	0.0291	0.0291	0.0291	F
			0.0208	0.0265	0.0284	0.0289	0.0290	0.0290	0.0291	S1

(b)

kb	$a/b = 0$	0.2	0.5	0.7	0.9	Mode
0.3	0.0237	0.0237	0.0234	0.0228	0.0215	F
	0.0352	0.0351	0.0344	0.0329	0.0309	S1
0.37276613	0.0291	0.0291	0.0291	0.0291	0.0291	F
	0.0291	0.0290	0.0275	0.0241	0.0155	S1

TABLE 3. Predicted linear growth rates, $S = s\gamma/(\mu b)$. (a) Growth rates for a pure thread. The penultimate column headed by infinity denotes the exact value obtained by Tomotika (1935) in terms of Bessel functions. In the last column, F denotes the fundamental wave, and S1 denotes the first higher harmonic. The Green's function computational parameter N_G is defined in Appendix B. (b) Effect of particles on the growth rate of dominant normal modes. These growth rates were computed with $\epsilon = 10^{-6}$, $N_G = 3$, $N_P = 32$ and $N_I = 96$ for $kb = 0.3$ or $N_I = 128$ for $kb = 0.37276613$.
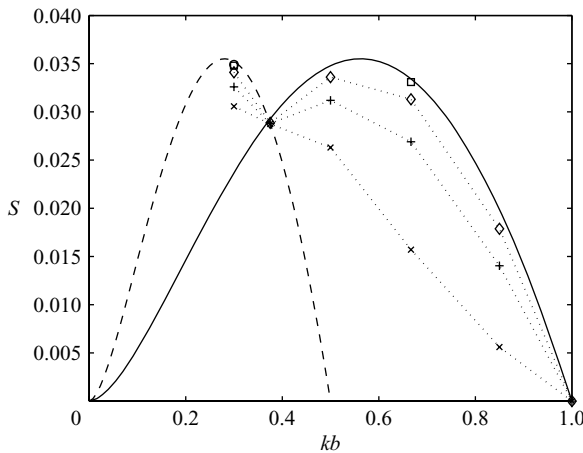

FIGURE 8. Reduced growth rate, $S = s\gamma/(\mu b)$, of axisymmetric perturbations on a pure thread of radius b with sinusoidal waves of wavelength L (solid line) and its first higher harmonic (dashed line). The symbols mark the dominant growth rate for $kb = 0.3$, 0.375, 0.5, 2/3, 0.85 and 1 and particle radius $a/b = 0.05$ ($\bigcirc$), 0.20 ($\square$), 0.50 ($\diamond$), 0.70 (+) and 0.90 (×).

To validate the method, we consider the capillary instability of a pure thread of radius b, in the absence of particles. Tomotika's (1935) exact growth rates are plotted with the solid line in figure 8. Table 3(a) summarizes the dominant growth rates computed by the numerical linear stability analysis for three wavenumbers. For a fixed configuration, the numerical error is of the order of the magnitude of the

numerical impulse, ϵ. When $kb = 2/3$, only one positive eigenvalue appears, and all higher harmonics are stable. When $kb = 0.3$, two positive eigenvalues appear, one corresponding to the fundamental wave (F) and the second corresponding to its first higher harmonic wave (S1); higher harmonics are stable. When $kb = 0.37276613\ldots$, the growth rates of the fundamental wave are identical; higher harmonics are stable. The numerical results demonstrate a rapid convergence with the known analytical solution as the number of interfacial elements becomes higher.

In the case of a pure thread, the eigenvectors of the interfacial displacement are pure sinusoidal waves. The growth rates may then be extracted by imposing a discrete small-amplitude sinusoidal perturbation and identifying the growth rate with the ratio between the radial velocity and radial displacement of each node. A node-averaged value may be defined in some sensible fashion to filter out numerical noise. Numerical experiments have shown that the numerical linear stability analysis in terms of the matrix **M** presented in this section is superior, in that the averaging occurs naturally through the computation of the eigenvalues. Consequently, the results converge faster with respect to the number of intervals, and the predictions are less sensitive to the evaluation accuracy of the periodic Green's function.

Table 3(b) presents growth rates furnished by the numerical stability analysis for a particle-laden thread. For $kb = 0.3$, the predicted growth rates are less than those of the pure thread. The results for $a/b = 0.2$ are consistent with those of the stability analysis based on a Fourier series expansion discussed in §3. Due to the large number of terms required to capture the fine features of the eigenfunctions, the Fourier solution is not able to yield reliable results for particles whose radius is approximately larger than one fifth of the thread radius. The results for $kb = 0.37276613\ldots$ are astonishing. We find that the growth rate of the fundamental wave remains locked at the pure-thread value, at least up to the third significant figure, for any particle radius. By contrast, the growth rate of the first higher harmonic exhibits a strong dependence on the particle radius. This behaviour can be attributed to some type of resonance whose physical origin could not be identified.

Figure 9 shows graphs of the eigenfunctions of the dominant normal modes representing interfacial displacements for $kb = 2/3$ and 0.3 and four particle sizes. When $kb = 2/3$, the fundamental wave dominates. When $kb = 0.3$, the first higher harmonic wave dominates. The virtually imperceptible dashed lines in the first two frames of figure 9(b) represent the predictions of the Fourier linear stability theory discussed in §3. The successful comparison confirms the accuracy of both the Fourier analysis and boundary integral formulation. Consistent with physical intuition, as the particle size increases, the interface deforms less over the particle, located at $x = 0$, than in the intervening region. The effect for large particles is manifested as a localized downward indentation in the interfacial deformation above the particle surface.

The effect of the particles on the dominant growth rate is summarized by the graphs connecting the symbols in figure 8. For a fixed particle separation, the larger the particle radius the smaller the growth rate. We have seen that the particle spacing in which the growth rates of the fundamental wave (solid line) and its first higher harmonic wave (dashed line) on the pure thread are equal, corresponding to $kb = 0.37276613\ldots$, is special. When the wavenumber lies on the right of the intersection, the growth rates of the particle-laden thread fall on a locus that arises from the downward displacement of the pure-thread lobe. When the wavenumber lies on the left of the intersection, the growth rates arise from the downward displacement of the first higher harmonic of the pure thread, and corresponding eigenfunctions contain strong higher harmonic components, as illustrated in figure 9. For any particle size, the growth rate curves tracing the symbols in figure 8 converge at the
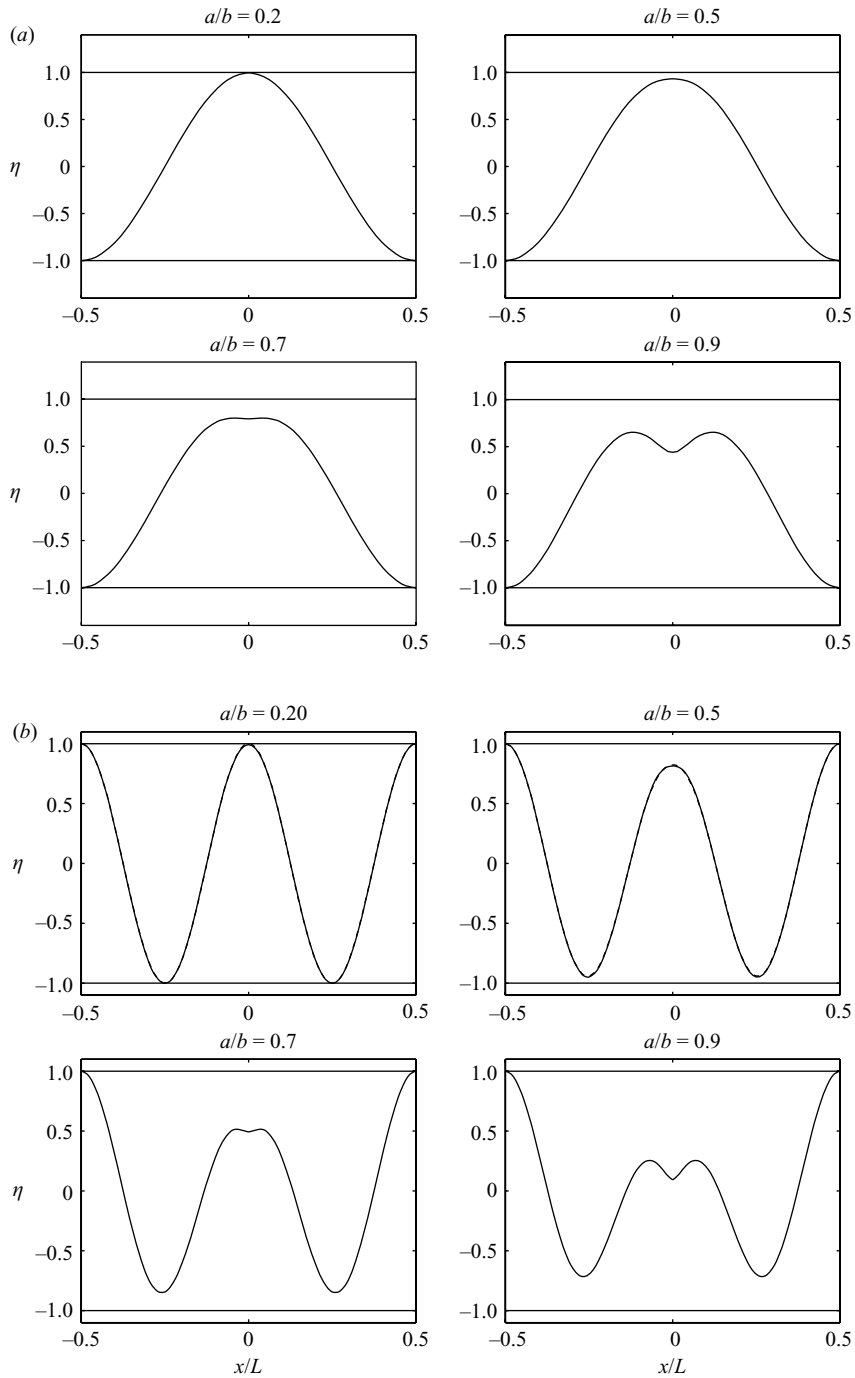
FIGURE 9. Eigenfunctions of the dominant normal modes for four particle radii and fundamental wavenumbers (*a*) $kb = 2/3$ and (*b*) 0.3. The centre of one particle is located at the origin of the *x*-axis.
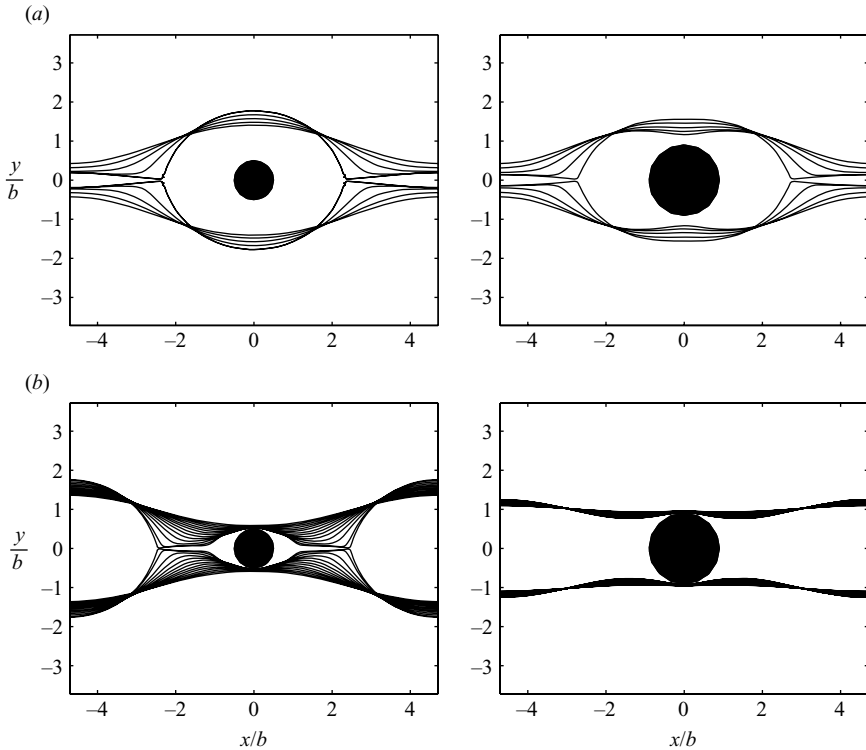
FIGURE 10. Evolving profiles of the unstable thread for $kb = 2/3$ and particle radius $a/b = 0.5$ (left) and 0.9 (right). In (*a*), the initial perturbation peaks over the particles (peaked configuration). In (*b*), the initial perturbation reaches a trough over the particles (depressed configuration).

intersection. These results are consistent with those obtained by the Fourier linear stability analysis. The extension to larger particle sizes demonstrates the strong effect of particles occupying a significant portion of the cross-section of the thread.

5.2. *Dynamic simulations*

To describe the nonlinear stages of the instability, we perform dynamical simulations using as an initial condition the normal-mode interfacial profiles of the most unstable modes available from the numerical linear stability analysis discussed in §5.1. In the numerical method, the integral equation for the particle traction is solved; the interfacial velocity is computed; and the position of the interfacial nodes is advanced in time using the first- or second-order Runge–Kutta method. To ensure adequate resolution and prevent node clustering, interfacial marker points are adaptively redistributed after each time step. The algorithm maintains the local aperture angle subtended by the centre of curvature below a specified threshold and ensures that the arclength between two successive points lies inside a specified window. Closely spaced points are removed, provided that the specified level of spatial resolution is not violated. When new interfacial nodes are introduced, their position is computed from the cubic spline interpolation. The simulations end when the thread thins to the point of impending breakup indicated by artificial interfacial crossing.

Figure 10 shows evolving profiles of the unstable thread for particle separations corresponding to $kb = 2/3$ and particle radius $a/b = 0.5$ and 0.9. In figure 10(*a*),
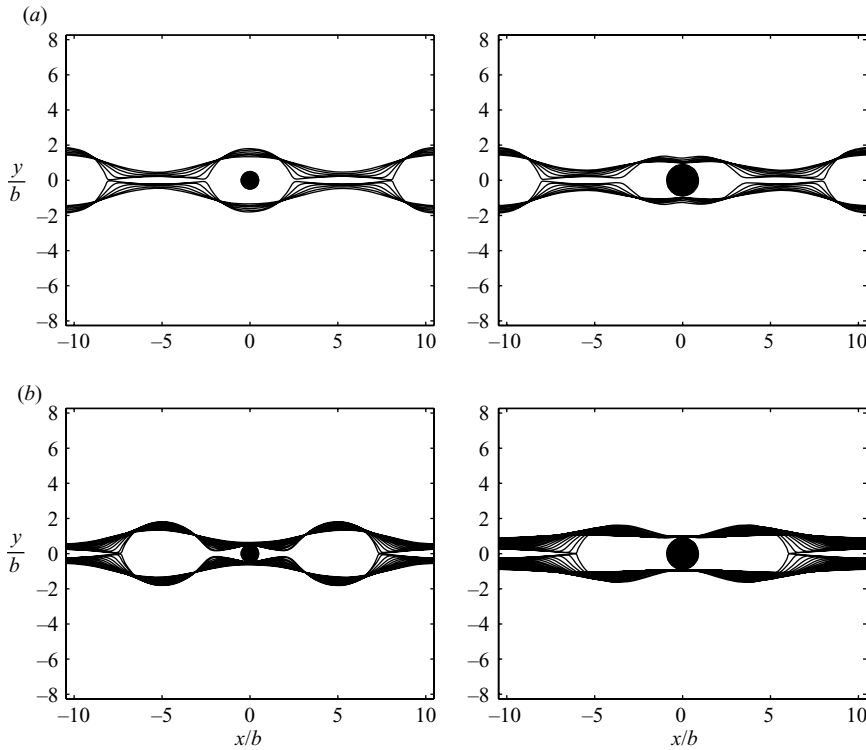
FIGURE 11. Same as figure 10 but for $kb = 0.3$.

the initial perturbation peaks over the particles (peaked configuration), whereas in figure 10(*b*), the initial perturbation reaches a trough over the particles (depressed configuration). The initial interfacial shape is a sinusoidal wave with amplitude 0.5*b* in both configurations shown in figure 10(*a*) and amplitude 0.4*b* and 0.1*b*, respectively, in the first and second configuration shown in figure 10(*b*). As the instability develops in the peaked configuration, large drops engulf the particles, and slender thinning ligaments develop in the intervening region. The particle size has a moderate effect on the interfacial morphology and distribution of the fluid between the encapsulated particles and connecting ligaments. Ligament breakup occurs at a finite time, leading to the formation of small satellite drops.

In the depressed configuration illustrated in figure 10(*b*), small drops engulf moderate-sized particles with $a/b = 0.5$, while large pure drops connected by ligaments develop in the intervening regions. When $a/b = 0.9$, the instability is nearly suppressed, as the interface approaches the particle surface to form a sequence of particles connected by axisymmetric bridges. The emerging configuration is similar to that of a liquid bridge held by the the particle surfaces emulating fixed endplates. Because $kb < 1$, the bridge is linearly unstable and is expected to disintegrate at long time periods. However, the growth rate of the instability is significantly lower than that of the homogeneous thread.

Figure 11 shows evolving profiles of an unstable thread for a larger particle separation corresponding to $kb = 0.3$. In the peaked configuration shown in figure 11(*a*), the thread is eventually divided into two alternating arrays of drops, only one of which encapsulates particles, while an amount of fluid escapes into the ligaments. In

the depressed configuration shown on the left of figure 11(*b*), the vast majority of the fluid escapes into empty drops. Thus, two different coating thicknesses are expected to arise after encapsulation. It is striking that in the case of large particles, illustrated in the right column of figure 11, peaked and depressed perturbations lead to radically different structures. In the second case, it appears that two nearly stationary drops attached to the particle develop on either side.

6. Discussion

We have considered the capillary instability of a liquid thread encapsulating a regular array of spherical particles, and we have described the properties of exponentially growing or decaying linear normal modes. The mathematical formulation is challenging in that the interfacial perturbation and disturbance flow are not sinusoidal waves but are described instead by polychromatic Fourier series expansions. The fundamental wave is determined by the particle spacing, and the Fourier spectrum is determined by the particle size. In the absence of particles, only the fundamental wave survives.

The pure thread is unstable only when the fundamental wavenumber reduced by the inverse of the undeformed thread radius is smaller than unity. We have confirmed that the same holds true for a thread loaded with particles. As the particle spacing increases, the particles play an increasingly important role by determining the most unstable available higher harmonic wave. At a predictable sequence of wavenumbers, the interfacial deflection of the loaded thread is composed solely of contributions from the higher harmonics of the fundamental wave. Correspondingly, the growth rate approaches a finite limit as the particle spacing grows. An insoluble surfactant generally lowers the growth rate of the normal modes. However, the surfactant is not able to completely stabilize the thread. These results are consistent with the findings of Kwak & Pozrikidis (2001) for a pure thread devoid of particles. A loaded thread becomes more unstable when suspended in a less viscous fluid. A thread suspended in a vacuum shows markedly different behaviour when clean or contaminated with surfactant.

We have developed a boundary integral formulation to describe the capillary instability of a particle-laden thread subject to axisymmetric perturbations. The numerical method was successfully applied to carry out a numerical linear stability analysis, yielding the growth rates and waveforms of fundamental and higher harmonic waves. The methodology is not unique to the thread but can be generalized to arbitrary configurations involving interfaces between immiscible fluids. An example is the stability of a pendant axisymmetric liquid drop or liquid bridge subtended between two concentric cylinders.

The linear stability analysis performed with the boundary integral method has confirmed the results produced by the Fourier series analysis. Excellent agreement was confirmed for small particles whose radius was up to one fifth of the thread radius. The boundary integral method was applied to compute growth rates for different particle sizes and particle spacings. Most interestingly, the calculations confirmed the intriguing observation that when the particle spacing takes a special value corresponding to the wavenumber at which the growth rates of the fundamental mode for a pure thread and its first higher harmonic coincide, the growth rate of the dominant mode does not depend on the particle size. At other wavenumbers, the particle size has a significant effect on the linear displacement of the interface. In particular, for larger particles and fixed particle separation, the interfacial deflection is considerably smaller than midway between the particles.

Dynamic simulations performed with the boundary element method have illustrated the progress of the instability in the nonlinear regime in which the interfacial deflection is not small, for fluids with equal viscosity. Experience with similar problems involving liquid drops suggests that the motion for $\lambda = 1$ is representative of that for approximately $0 < \lambda < 5$. (e.g. Kennedy, Pozrikidis & Skalak 1994). For an initial profile that peaks over a moderate-sized particle, the latter stages of the evolution are characterized by large drops of fluid encapsulating the particle and linked by thin fluid strands that tend to pinch off at the point at which they connect to the drops. For an initial profile with a trough over a moderate-sized particle, the latter stages of the evolution are characterized by small drops of fluid encapsulating the particle, linked by short strands to much larger drops of clear fluid on either side. The nonlinear outcome of the encapsulation process depends crucially on the form of the initial perturbation.

Appendix A. Computation of derivatives of the point force and point source

In this appendix, we supply recurrence relations used to efficiently compute the derivatives arising in the expressions for the point force, $\mathscr{S}_3$, in (3.8) and for the point source, $\mathscr{S}_5$ in (3.10). For the point force, we define

$$\mathscr{S}_3 \equiv \sum_{n=-\infty}^{\infty} s_3, \qquad s_3 = \frac{\hat{x} - n\hat{L}}{P}, \tag{A 1}$$

where $P = Q^3$ with

$$Q = [\hat{\sigma}^2 + (\hat{x} - n\hat{L})^2]^{1/2}. \tag{A 2}$$

Multiple differentiation of (A 2) yields the formula

$$\frac{\partial^r Q}{\partial \hat{x}^r} = \frac{1}{Q} \left\{ \frac{\partial^{r-1}}{\partial \hat{x}^{r-1}}(\hat{x} - n\hat{L}) - \frac{1}{2} \sum_{p=1}^{r-1} \binom{r}{p} \frac{\partial^p Q}{\partial \hat{x}^p} \frac{\partial^{r-p} Q}{\partial \hat{x}^{r-p}} \right\} \tag{A 3}$$

for $r \geqslant 1$, where the summation term is ignored in the case $r = 1$. Straightforward manipulation of the preceding expressions produces the pair of recurrence relations,

$$\frac{\partial^r P}{\partial \hat{x}^r} = 3(\hat{x} - n\hat{L})\frac{\partial^{r-1} Q}{\partial \hat{x}^{r-1}} + 3(r - 1)\frac{\partial^{r-2} Q}{\partial \hat{x}^{r-2}} \tag{A 4}$$

for $r = 2, 3, \ldots$ and

$$\frac{\partial^k s_3}{\partial \hat{x}^k} = -\frac{1}{P} \left\{ \sum_{r=1}^{k} \binom{k}{r} \frac{\partial^{k-r} s_3}{\partial \hat{x}^{k-r}} \frac{\partial^r P}{\partial \hat{x}^r} + \frac{\partial^k}{\partial \hat{x}^k}(\hat{x} - n\hat{L}) \right\} \tag{A 5}$$

for $k = 1, 2, \ldots$.

For the point source, we define

$$\mathscr{S}_5 \equiv \sum_{n=-\infty}^{\infty} s_5, \qquad s_5 = \frac{x - n\hat{L}}{R}, \tag{A 6}$$

where $R = Q^5$, and derive the recurrence relations

$$\frac{\partial^r R}{\partial \hat{x}^r} = 5(\hat{x} - n\hat{L})\frac{\partial^{r-1} P}{\partial \hat{x}^{r-1}} + 5(r-1)\frac{\partial^{r-2} P}{\partial \hat{x}^{r-2}} \tag{A 7}$$

for $r = 2, 3, \ldots$ and

$$\frac{\partial^k s_5}{\partial \hat{x}^k} = -\frac{1}{R}\left\{\sum_{r=1}^{k}\binom{k}{r}\frac{\partial^{k-r} s_5}{\partial \hat{x}^{k-r}}\frac{\partial^r R}{\partial \hat{x}^r} + \frac{\partial^k}{\partial \hat{x}^k}(\hat{x} - n\hat{L})\right\} \tag{A 8}$$

for $k = 1, 2, \ldots$.

Appendix B. Computation of the periodic Green's function of Stokes flow

To develop the boundary integral formulation of the axisymmetric thread breakup, we introduce the free-space Green's function of axisymmetric Stokes flow defined such that

$$u_\alpha^R(\boldsymbol{x}_0) = -\frac{1}{8\pi\mu}G_{\alpha\beta}^{FS}(\boldsymbol{x}, \boldsymbol{x}_0)g_\beta \tag{B 1}$$

is the velocity at the point $\boldsymbol{x}_0$ induced by a ring of point forces of radius σ positioned at $\boldsymbol{x}$; μ is the fluid viscosity; g_β is the strength of the point force ring; and Greek indices can be x or σ. An analytical expression for the Green's function in terms of complete elliptic integrals accompanied by computer programmes is available (e.g. Pozrikidis 1992, 2001). It can be shown that the free-space Green's function satisfies the symmetry property

$$\sigma_0 G_{\beta\alpha}^{FS}(\boldsymbol{x}, \boldsymbol{x}_0) = \sigma G_{\alpha\beta}^{FS}(\boldsymbol{x}_0, \boldsymbol{x}), \tag{B 2}$$

which allows us to switch the position of the evaluation point and the point-force ring. Thus, the velocity due to the ring can be expressed in the alternative form

$$u_\alpha^R(\boldsymbol{x}) = -\frac{\sigma}{8\pi\mu\sigma_0}g_\beta G_{\beta\alpha}^{FS}(\boldsymbol{x}_0, \boldsymbol{x}). \tag{B 3}$$

Mass conservation requires an integral identity stemming from the continuity equation,

$$\oint_C n_\alpha(\boldsymbol{x}_0)G_{\alpha\beta}^{FS}(\boldsymbol{x}, \boldsymbol{x}_0)\sigma_0 \mathrm{d}l(\boldsymbol{x}_0) = 0, \tag{B 4}$$

where C is a closed contour in a meridional plane possibly involving a section of the x-axis; $\boldsymbol{n}$ is the unit vector normal on C; and l is the arclength along C. Using the symmetry identity and then relabeling $\boldsymbol{x}$ as $\boldsymbol{x}_0$ and vice versa, we find

$$\oint_C G_{\alpha\beta}^{FS}(\boldsymbol{x}, \boldsymbol{x}_0)n_\beta(\boldsymbol{x})\mathrm{d}l(\boldsymbol{x}) = 0. \tag{B 5}$$

Thus, the normal vector is an eigenfunction corresponding to the null eigenvalue of the single-layer potential of axisymmetric Stokes flow,

$$\mathscr{I}_\alpha^{SLP} < \psi > \equiv \oint_C G_{\alpha\beta}^{FS}(\boldsymbol{x}, \boldsymbol{x}_0)\psi_\beta(\boldsymbol{x})\mathrm{d}l(\boldsymbol{x}). \tag{B 6}$$

That is, $\mathscr{I}_\alpha^{SLP} < \boldsymbol{n} > = 0$.

N_G	G_{xx}	$G_{x\sigma}$	$G_{\sigma x}$	$G_{\sigma\sigma}$
1	-10.0939	-1.5496	-0.6979	-4.4348
2	-9.2954	-1.0892	-0.8799	1.2583
3	-9.2292	-1.1093	-0.8554	1.3077
4	-9.2172	-1.1120	-0.8525	1.3151
5	-9.2139	-1.1127	-0.8518	1.3170
6	-9.2127	-1.1129	-0.8516	1.3177
7	-9.2122	-1.1130	-0.8515	1.3180
8	-9.2120	-1.1131	-0.8515	1.3181
9	-9.2118	-1.1131	-0.8514	1.3182
10	-9.2117	-1.1131	-0.8514	1.3183

TABLE 4. Convergence of the periodic Green's function for axisymmetric flow with respect to the truncation level, p, for $L/\sigma = 1$, $x_0 - x = 0.1\sigma$ and $\sigma_0 = 0.9\sigma$. The last row is accurate to the fourth decimal place.

To obtain the flow due to a periodic array of point-force rings separated by the distance L, we apply direct summation and find

$$G_{\alpha\beta}(\boldsymbol{x}, \boldsymbol{x}_0) = \sum_{n=-\infty}^{\infty} G_{\alpha\beta}^{FS}(x + nL, \sigma, x_0, \sigma_0). \qquad (\text{B}\,7)$$

The summed terms in (B 7) decay like $1/|nL|^2$ for all but the xx component of the Green's function, and the corresponding infinite sums are convergent. The summed terms for G_{xx}^{FS} decay like $1/|nL + x - x_0|$, and the corresponding sum is divergent, requiring renormalization. However, since the x velocity at the point $\boldsymbol{x}_0$ can be modified by an arbitrary constant that is independent of $\boldsymbol{x}_0$ but may depend on x and σ, we write

$$G_{xx}(\boldsymbol{x}, \boldsymbol{x}_0) = \sum_{n=-\infty}^{\infty} G_{xx}^{FS}(x + nL, \sigma, x_0, \sigma_0) - 8\pi\sigma \sum_{n=1}^{\infty} \frac{1}{|nL|}. \qquad (\text{B}\,8)$$

The combined summed terms now decay like $1/|nL|^2$ for all components of the periodic Green's function. To expedite the convergence, we truncate the sums at $N = q^2 N_G$, where N_G and q are two integers, and use the intermediate sums for $N = N_G$ and $N = qN_G$ to perform Aitken extrapolation (Pozrikidis 2008). The fast convergence of the expedited summation is demonstrated in table 4 for a particular configuration. In the numerical simulations discussed in §5, we choose $q = 2$ and adjust the value of N_G according to the separation, L, and the ring radius, σ, to achieve a specified level of accuracy.

REFERENCES

BLYTH, M. G. & POZRIKIDIS, C. 2004 Evolution equations for the surface concentration of an insoluble surfactant: stability of an elongating thread and a stretched interface. *Theor. Comp. Fluid Dyn.* **17**, 147–164.

GOOSEN, M. F. A., O'SHEA, G. M., GHARAPETIAN, H. M., CHOU, S. & SUN, A. M. 1985 Optimization of microencapsulation parameters: semipermeable microcapsules as a bioartificial pancreas. *Biotechnol. Bioengng* **27** (2), 146–150.

GOREN, S. L. 1962 The instability of an annular layer thread of fluid. *J. Fluid Mech.* **12**, 309–319.

HATZIAVRAMIDIS, D. 2006 *A Device for Encapsulation of Living Cells or Cell Aggregates*. US patent disclosure.

HATZIAVRAMIDIS, D. & POZRIKIDIS, C. 2007 Hydrodynamic analysis of pancreatic islet micro-encapsulation by selective withdrawal. *Eng. Anal. Bound. Elem.* **32**, 11–20.

KENNEDY, M., POZRIKIDIS, C. & SKALAK, R. 1994 Motion and deformation of liquid drops, and the rheology of dilute emulsions in shear flow. *Comp. Fluids* **23**, 251–278.

KWAK, S. & POZRIKIDIS C. 2001 Effect of surfactants on the instability of a liquid thread or annular layer. Part I. Quiescent fluids. *Intl J. Mult. Flow* **27**, 1–37.

LI, X. & POZRIKIDIS, C. 1997 Effect of surfactants on drop deformation and on the rheology of dilute emulsions in Stokes flow. *J. Fluid Mech.* **341**, 165–194.

ORIVE, G., HERNANDEZ, R. M., GASCON, A. R., CALLAFIORE, R, CHANG, T. M. S., HORTELANO, G., HUNKELER, D., LACIK, I., SHAPIRO, A. M. J. & PEDRAZ, J. L. 2003 Cell encapsulation: promise and progress. *Nature Med.* **9**, 104–107.

POZRIKIDIS, C. 1992 *Boundary Integral and Singularity Methods for Linearized Viscous Flow.* Cambridge University Press.

POZRIKIDIS, C. 1997 *Introduction to Theoretical and Computational Fluid Dynamics.* Oxford University Press.

POZRIKIDIS, C. 2004 Instability of multi-layer channel and film flows. *Adv. Appl. Mech.* **40**, 179–239.

POZRIKIDIS, C. 2008 *Numerical Computation in Science and Engineering, I: Numerical Methods.* Oxford University Press.

TOMOTIKA, S. 1935 On the instability of a cylindrical thread of a viscous liquid surrounded by another viscous fluid. *Proc. R. Soc.* A **150**, 322–337.

WANG, H. & SKALAK, R. 1969 Viscous flow in a cylindrical tube containing a line of spherical particles. *J. Fluid Mech.* **38**, 75–96.

YON, S. & POZRIKIDIS, C. 1998 A finite-volume/boundary-element method for interfacial flow in the presence of surfactants, with applications to shear flow past a viscous drop. *Comp. Fluids* **27**, 879–902.